Solar Radiation Pressure Enabled Femtosatellite Based Earth Remote Sensing

J. Cao, C. Clemente, *Member, IEEE,* C. R. McInnes, and J. J. Soraghan, *Senior Member, IEEE*

***Abstract*—Recent developments in electronics have pushed miniaturised satellites to the femto-scale, with masses between 10 and 100 g. Although femtosatellites have been proven as a feasible concept, most designs are limited in mission capacity and lifetime due to the lack of environmental protection and onboard propellant. In this paper, a novel concept for femtosatellites for Earth remote sensing is proposed. In particular, a swarm of femtosatellites are used as elements of a sparse array in orbit to receive radar echoes. They also feature active orbit control enabled by solar radiation pressure to extend their lifetime. A simple active orbit control algorithm has been demonstrated. A mission concept based on a Sun-synchronous circular orbit is proposed to maximise the benefit for both Earth remote sensing and active orbit control. A synthetic aperture radar mission has been used to characterise their performance.**

***Index Terms*—Femtosatellite, Solar sailing, Relative motion, Earth remote sensing, Bi-static synthetic aperture radar.**

I. Introduction

The concept of femtosatellites first emerged in the West Ford Experiment in May 1963, during which a cloud of needles was used as an artificial reflection layer for 8 GHz radio signals [1]. In total, 480 million copper needles, which were 18 mm long and 0.018 mm diameter, were launched in the experiment. After two months, the needles spread to a 30 km thick and 15 km wide cloud at 3700 km altitude. Thirty years later, feasible and cost-effective solutions for femtosatellites were introduced as the "satellite-on-a-chip" concept in 1994 [2]. Subsequently, many concepts were proposed, such as the Co-Orbiting Satellite Assistant (COSA), PCBSat, WikiSat, and Sprite from KickSat project [3]–[6].

Solar sailing is a form of spacecraft propulsion using solar radiation pressure, generating acceleration from the momentum of solar photons. Compared to conventional propulsion, there is no onboard propellant, which can further reduce the mass and volume of femtosatellites. Solar radiation pressure can be controlled using electrochromic panels [7], [8]. This enables femtosatellites to take advantage of solar radiation pressure for orbit control. This paper will therefore investigate the use of solar radiation pressure for active orbit control to increase the capability of swarms of femtosatellites for radar applications. An early version of the concept has been published in [11].

Earth remote sensing is one of the most popular space-based radar missions. Since optical sensor performance varies with atmospheric conditions, a radar-based sensing system may on the other hand provide enhanced capability and acquire data regardless of weather and lighting conditions. A standard radar system includes a signal source, so it operates night and day, unlike most optical sensors which depend on Sun-illuminated surfaces. Synthetic Aperture Radar (SAR) exploits the sensor's motion in order to produce high resolution images of areas of interest [12]. Instead of using a large real aperture antenna, SAR uses a large virtual antenna that is formed by relative motion between the radar and target to achieve high-resolution images. The time delay is the combination of the transmitter-to-target and target-to-receiver delay. In earlier remote sensing applications, a radar would provide range to objects and surfaces by calculating the delay of a signal between the radar and the target. Subsequently, Doppler shift was implemented in radar systems to measure the speed of the target. Doppler shift has also been used to achieve higher spatial resolution in a direction perpendicular to the beam direction. A wide range of Earth remote sensing applications based on SAR technology have been investigated and implemented [13]–[15]. The first microsatellite with SAR application, ICEYE-X1, was launched in January 2018 [16].

This paper combines femtosatellites, solar sailing for active orbit control and SAR concepts for a novel radar application using a femtosatellite swarm. The swarm of femtosatellites act as passive receivers and a carrier spacecraft as a transmitter where the constellation can be classified as a bi-static radar configuration. In radar systems, mono-static and bi-static denote the location of the transmitter and the receiver, where mono-static indicates that they are co-located and bi-static that they are separated. Compared to a mono-static SAR system, bi-static SAR receives echoes from different locations which provide the possibility of extracting more information by implementing advanced radar signal processing [17]. The femtosatellites are released from the carrier spacecraft and maintained within a certain range by solar radiation pressure control. Compared to conventional configurations, this increases the lifetime of the femtosatellites and reduces their total weight by using active orbit control to recycle the femtosatellites. The subsequent processed radar images can be used for Earth remote sensing and target detection. Such a system could detect ships, whose automatic identification system (AIS) is turned off, or airliners without a beacon signal when combined with information from other sources [18]. This system can be used for future maritime and aviation security applications, for quick response in disaster monitoring and space debris detection [19]. We envisage the system as hibernating in orbit with the swarm deployed from the car-

J. Cao, C. Clemente, and J. J. Soraghan are with the University of Strathclyde, G1 1XW, Glasgow, UK. E-mail: jianlin.cao, carmine.clemente, j.soraghan- @strath.ac.uk

C. R. McInnes is with the University of Glasgow, G12 8QQ, Glasgow, UK. E-mail: colin.mcinnes@glasgow.ac.uk

rier in emergency search situations with discrete observation periods. A simple model of the solar radiation pressure and aerodynamics forces are provided for ease of illustration to assess the concept presented.

The remainder of the paper is organised as follows. A preliminary design of the femtosatellite prototype for the novel radar mission is introduced in Section II. The dynamics of the femtosatellite is described in Section III with an example scenario evaluated. In order to further prove the utility of femtosatellites, the bi-static synthetic aperture radar application for Earth remote sensing will be discussed in Section IV. Section V concludes the paper.

II. Femtosatellite Design

A preliminary design of the femtosatellite prototype is introduced in this section. Based on previous concepts for femtosatellites [3]–[6], a design has been developed to provide an acceptable level of mission capability and environment survivability for a swarm radar mission [11]. The proposed design is composed of a flat-bubble shape, as shown in Figure 1. The femtosatellite is built on Kapton film as an alternative to a printed circuit board to reduce weight and provide flexibility. The extended Kapton film covers the core electronics to protect them from radiation and provides passive thermal control. The thin-film solar panel around the edges are not covered to maximise the solar power output.

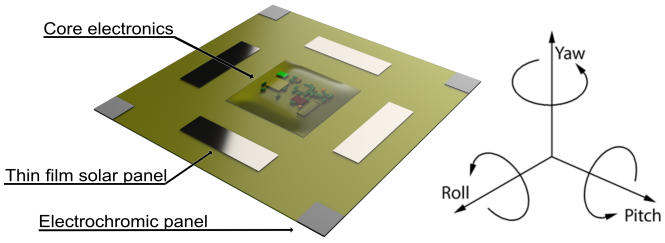

Fig. 1: Flat-bubble shaped prototype concept

This design features a high area-to-mass ratio which enables the femtosatellites to take advantage of solar radiation pressure for propulsion without onboard propellant. Electrochromic panels in each corner can be controlled to change their transparency, from transparent to black to enable attitude control [8]–[10]. [1] Size and weight are minimised by integrating subsystems together to provide additional payload capacity. It can be also re-configured as a relay to extend the communication range of an individual device while 'on-the-fly'. Although the subsystems are highly integrated, all components can be obtained as commercial off-the-shelf (COTS) products to reduce the cost [11].

In order to maximise the benefits of solar radiation pressure for orbit control and to maintain a high area-to-mass ratio, flat micro-strip antennae and surface-mount chip antennae are considered for radar applications and communication. According to the orbit and the required attitude of the femtosatellite, the antenna design will vary. The design could vary from a single or array design depending on the radar carrier frequency and beam-form requirements. The antennae could also be placed symmetrically and controlled by electric relays to reduce attitude manoeuvres in the yaw axis. A surface-mount chip antenna is assumed to be used for communication between femtosatellites and the carrier spacecraft. It features a smaller footprint and a more stable performance than other commonly used antennas. A communication link to the carrier spacecraft is essential for the femtosatellite to transmit its position and receive a signal back at the carrier spacecraft. A commercial GPS chip is assumed to be used for positioning, although in principle computer vision at the carrier spacecraft could be used to enhance the femtosatellite relative positioning.

Similar to other small satellites, the main limitation on femtosatellite performance is low battery power density. Therefore, a 'dawn-dusk' Sun synchronous orbit will be considered which is frequently used in Earth remote sensing missions to provide constant solar flux without an eclipse. The orbit plane remains perpendicular to the incoming solar radiation in the dawn-dusk orbit. The femtosatellites would be under direct illumination during the entire orbit to maximise power generation and enable solar radiation pressure for orbit control. In order to take the full advantage of the Sun-synchronous orbit remote sensing, a Vivaldi antenna is used. Compared to commonly used antennae, where the direction of the main lobe is parallel to the antenna normal, the Vivaldi antenna has a main lobe perpendicular to its normal [20]. The femtosatellite yaw control can be simplified with four individual antennae on each edge.

III. Femtosatellite Dynamics

As noted in the introduction, the Earth remote sensing mission proposed in this paper is a bi-static synthetic aperture radar mission which includes a swarm of the femtosatellites as passive receivers and a carrier spacecraft as the transmitter. Therefore, this section will focus on the relative motion between the carrier spacecraft and the femtosatellites.

The periodic motion between two close objects in the space environment within a relatively short distance is termed relative motion. It shares the same period as the period of the reference orbit around the Earth. A coordinate system is introduced in Figure 2 to describe such relative motion [11]. The x-axis is perpendicular to the Earth's surface from the centre of the Earth, the y-axis is aligned with the velocity vector of the main carrier spacecraft and the z-axis completes the triad. The carrier spacecraft is located at the origin (0,0,0) of this local frame of reference.

All femtosatellites are assumed to be in nearly circular orbits. The simplified linear equations of relative motion with external accelerations (a_x, a_y, a_z) can then be written in the form of the Clohessy-Wiltshire or Hill's equations [21]:

$$\ddot{x} - 2\omega_n \dot{y} - 3\omega_n^2 x = a_x \tag{1a}$$

$$\ddot{y} + 2\omega_n \dot{x} = a_y \tag{1b}$$

$$\ddot{z} + \omega_n^2 z = a_z \tag{1c}$$

[1] Yaw control can be achieved by utilizing MEMS reaction wheels which is not included in this paper.

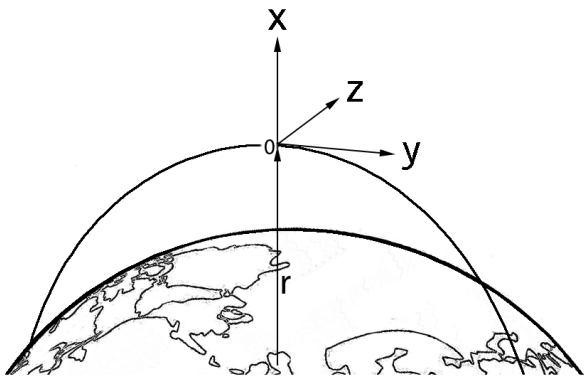

Fig. 2: Coordinate system geometry for relative motion

where:

$$\omega_n = \sqrt{\frac{\mu_{Earth}}{r^3}} \tag{2}$$

ω_n: mean angular motion
μ_{Earth}: gravitational parameter of the Earth ($3.986 \times 10^5\ km^3 s^{-2}$)
r: carrier spacecraft orbit radius

This relative motion model is used to describe the motion of femtosatellites under constant external accelerations. Solving Equation (1), an analytic solution for analysis and fast computation is found as follows:

$$\begin{aligned} x(t) = &\left(\frac{\dot{x}_0}{\omega_n} - \frac{2a_y}{\omega_n^2}\right)\sin(\omega_n t) \\ &- \left(3x_0 + \frac{2\dot{y}_0}{\omega_n} + \frac{a_x}{\omega_n^2}\right)\cos(\omega_n t) \\ &+ \frac{2a_y}{\omega_n}t + 4x_0 + \frac{2\dot{y}_0}{\omega_n} + \frac{a_x}{\omega_n^2} \end{aligned} \tag{3a}$$

$$\begin{aligned} y(t) = &\left(6x_0 + \frac{4\dot{y}_0}{\omega_n} + \frac{2a_x}{\omega_n^2}\right)\sin(\omega_n t) \\ &+ \left(\frac{2\dot{x}_0}{\omega_n} - \frac{4a_y}{\omega_n^2}\right)\cos(\omega_n t) \\ &- \frac{3a_y}{2}t^2 - \left(6\omega_n x_0 + 3\dot{y}_0 + \frac{2a_x}{\omega_n}\right)t \\ &+ y_0 - \frac{2\dot{x}_0}{\omega_n} + \frac{4a_y}{\omega_n^2} \end{aligned} \tag{3b}$$

$$z(t) = \frac{\dot{z}_o}{\omega_n}\sin(\omega_n t) + \left(z_0 - \frac{a_z}{\omega_n^2}\right)\cos(\omega_n t) + \frac{a_z}{\omega_n^2} \tag{3c}$$

$$\begin{aligned} \dot{x}(t) = &\left(3\omega_n x_0 + 2\dot{y}_0 + \frac{a_x}{\omega_n}\right)\sin(\omega_n t) \\ &+ \left(\dot{x}_0 - \frac{2a_y}{\omega_n}\right)\cos(\omega_n t) + \frac{2a_y}{\omega_n} \end{aligned} \tag{3d}$$

$$\begin{aligned} \dot{y}(t) = &-\left(2\dot{x}_0 - \frac{4a_y}{\omega_n}\right)\sin(\omega_n t) \\ &+ \left(6\omega_n x_0 + 4\dot{y}_0 + \frac{2a_x}{\omega_n}\right)\cos(\omega_n t) \\ &- 3a_y t - 6\omega_n x_0 - 3\dot{y}_0 - \frac{2a_x}{\omega_n} \end{aligned} \tag{3e}$$

$$\dot{z}(t) = -\left(\omega_n z_0 - \frac{a_z}{\omega_n}\right)\sin(\omega_n t) + \dot{z}_0\cos(\omega_n t) \tag{3f}$$

By integrating the Clohessy-Wiltshire equation (1b) without external acceleration ($a_y = 0$) as shown

$$\int \ddot{y}\ \mathrm{d}t + \int 2\omega_n \dot{x}\ \mathrm{d}t = c \tag{4}$$

it can be demonstrated that $\dot{y} + 2\omega_n x = c$ for some constant c.

Therefore a new parameter $\Gamma = \dot{y}_0 + 2\omega_n x_0$ can be defined which again is constant and evaluated at the initial conditions of the femtosatellite at release. When the femtosatellite is free-flying ($a_x = a_y = 0$), from Equation (3e) we can obtain

$$\dot{y}(t) = -2\dot{x}_0\sin(\omega_n t) + (6\omega_n x_0 + 4\dot{y}_0)\cos(\omega_n t) - 3\Gamma \tag{5}$$

So that, the long-term average speed in y-axis $\dot{y}(t)$ can be written as

$$\bar{\dot{y}}(t) = -3\Gamma \tag{6}$$

When $\Gamma = 0$, the femtosatellite will only have a periodic motion relative to the carrier spacecraft. This result will be used later to assess orbit control strategies.

A. Force Model

After ejection from the carrier spacecraft, typically with $\Gamma \neq 0$, the femtosatellites will drift away without active orbit control. By using the electrochromic panels on each corner, the femtosatellite can adjust its attitude to achieve active orbit control using solar radiation pressure. According to the analytic solution of the Clohessy-Wiltshire equations, the motion along the z-axis is decoupled from the x-axis and the y-axis. The lengthscale of motion along the y-axis is typically larger compared to the x-axis. According to Equation (3a) and (3b), the ratio of oscillation range between the y-axis and x-axis is 2:1 when $\Gamma = 0$. Therefore, an external force applied along the y-axis is used to constrain the distance between the femtosatellite and the carrier spacecraft to ensure a coherent swarm is established. This can be controlled via modulation of the attitude angle of the femtosatellite to the x, y-plane. The force model of the femtosatellites is shown in Figure 3, demonstrating the effect of solar radiation pressure (SRP) and atmospheric drag (AD).

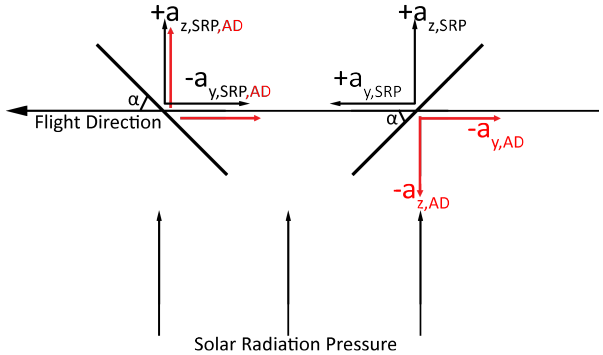

Fig. 3: Femtosatellite force model

Solar radiation pressure and atmospheric drag are the main external forces applied to both the femtosatellites and the

carrier spacecraft. The consequences of those two external forces are now considered. The total accelerations (Total) caused by the external forces are summarized as Equation (7), with carrier spacecraft acceleration (Carr) included, such that

$$\begin{cases} a_{y,\text{Total}} = a_{y,\text{SRP}} + a_{y,\text{AD}} - a_{y,\text{Carr}} \\ a_{z,\text{Total}} = a_{z,\text{SRP}} + a_{z,\text{AD}} - a_{z,\text{Carr}} \end{cases} \tag{7}$$

A simple model of the accelerations due to solar radiation pressure along the y-axis and z-axis are described in Equation (8), and detailed in Appendix A-A [21]. The sail efficiency, η, can be incorporated to represent the non-perfect optical properties of the femtosatellite surface although it is assumed the force is normal to the surface. The efficiency is assumed to be one to simplify the model [7], although [22] provides a detailed analysis of non-perfect conditions. The solar radiation pressure, P, is approximately $4.56 \times 10^{-6}\ Nm^{-2}$ in low Earth orbit [7]. The femtosatellite's mass and surface area are described by m and A. The femtosatellite's attitude angle in the x, y-plane along the x-axis is defined by α as shown in Figure 3, so that

$$\begin{cases} a_{y,\text{SRP}} = \dfrac{2\eta PA}{m} \cos^2\alpha \, \sin\alpha \\ a_{z,\text{SRP}} = \dfrac{2\eta PA}{m} \cos^3\alpha \end{cases} \tag{8}$$

A simple model of the aerodynamic forces are estimated using Equation (9) [21], [23], [24] and assumes free molecular flow and a Newtonian approximation, as detailed in Appendix A-B. Figure 4 shows the ratio of $a_{y,\text{AD}}$ to $a_{y,\text{SRP}}$ at various altitudes when $\alpha = 15°$. The atmospheric drag is the dominant force in the y-axis at lower altitudes, while radar applications favor lower altitudes to reduce the required transmit power and round trip signal loss. Therefore, 700 km is chosen as the orbit altitude for investigation in this paper. At 700 km altitude, the atmospheric density ρ is $3.614\times10^{-14} kg/m^3$ [21] and the relative speed v_{rel} is $7.5043\, km/s$. The femtosatellite used is assumed to be $0.02\ kg$ with an area of $0.01\ m^2$. It is noted that atmospheric density can vary significantly and so the relative magnitude of the solar radiation pressure force and aerodynamic forces will both vary and be uncertain. For the purposes of illustration, the density is assumed to be fixed, and again simple force models are used.

$$\begin{cases} a_{y,\text{AD}} = -\dfrac{A}{m}\rho v_{\text{rel}}^2 |\sin\alpha| \sin^2\alpha \\ a_{z,\text{AD}} = -\dfrac{A}{m}\rho v_{\text{rel}}^2 |\sin\alpha| \sin\alpha \, \cos\alpha \end{cases} \tag{9}$$

In addition to the effect of solar radiation pressure and atmospheric drag on the femtosatellite, the differential acceleration between the femtosatellite and the carrier spacecraft has been considered, which is described by Equation 10. The cross-section of the carrier spacecraft has been defined as $A_{\text{carrier},xz}$ for the y-axis and $A_{\text{carrier},xy}$ for the z-axis. The mass is m_{carrier}. The drag coefficient, $c_{D,normal}$, is considered to be approximately 2 for satellites in the upper atmosphere [21].

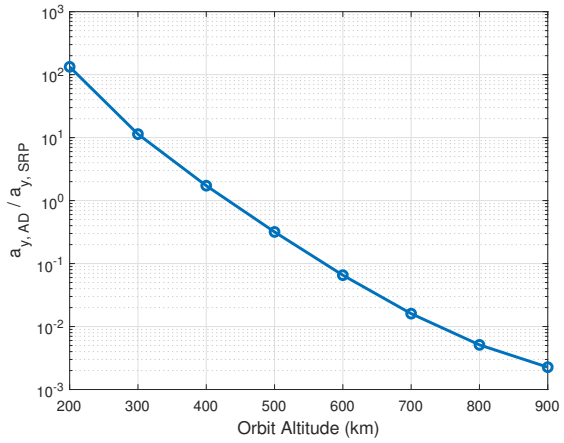

Fig. 4: Ratio of $a_{y,\text{AD}}$ to $a_{y,\text{SRP}}$ at various altitudes when α = 15°

In the coordinate system defined in Figure 2, where the origin of the local frame of reference is at the carrier spacecraft, the effect of forces applied on the carrier spacecraft can be considered equivalent to a reversed effect on the femtosatellite, so that

$$\begin{cases} a_{y,\text{Carr}} = -\dfrac{1}{2}\dfrac{c_D A_{\text{carrier},xz}}{m_{\text{carrier}}}\rho v_{rel}^2 \\ a_{z,\text{Carr}} = \dfrac{2\eta PA_{\text{carrier},xy}}{m_{\text{carrier}}} \end{cases} \tag{10}$$

A standard 3U CubeSat mass of 3 kg, cross-section $0.01\ m^2$ in the x, z-plane and $0.03\ m^2$ in the x, y-plane has been used as the carrier spacecraft and, again, femtosatellites of $0.02\ kg$ mass and $0.01\ m^2$ surface area for demonstration, with assumption that the carrier spacecraft will maintain its attitude with respect to the orbit. The external forces as a function of femtosatellite orientation are shown in Figure 5 and 6.

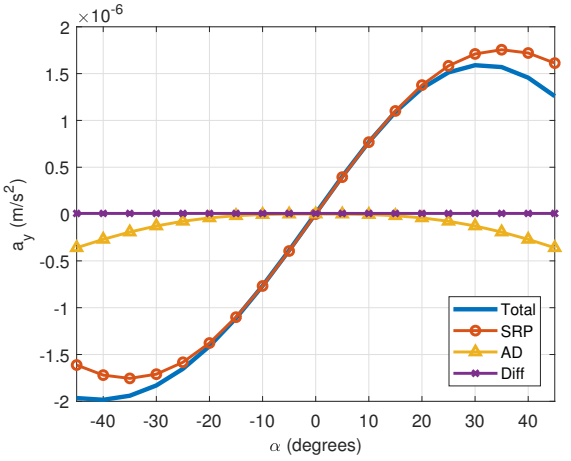

Fig. 5: Effect of atmospheric drag and solar radiation pressure along the y-axis

It can be seen that the effect of atmospheric drag is small relative to solar radiation pressure at the mission orbit altitude

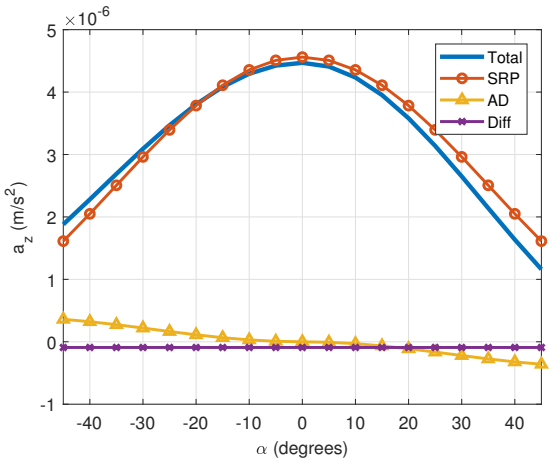

Fig. 6: Effect of atmospheric drag and solar radiation pressure along the z-axis

of 700 km. This provides the foundation of the capability for the femtosatellite to use solar radiation pressure for orbit control. Figure 5 shows that the total external force is minimised when $\alpha = 0$, which matches the design goal. For instance, when $\alpha \in (-15°, 15°)$, atmospheric drag is negligible where it contributes approximately 15% of total acceleration along the y-axis. As a result of atmospheric drag, the maximum magnitude of a_y in the $+y$ and $-y$ directions is at $\alpha = 31°$ and $\alpha = -41°$ respectively. This will be the operating range of α for maximum manoeuvrability. The atmospheric drag and differential drag will have a significant influence on the long-term orbit evolution, therefore it is necessary to consider these forces when planning a long-term mission. The influence of these drag forces can be overcome by active orbit control. Based on Equation (3c), the maximum displacement in the z-axis due to solar radiation pressure is $z_{max} = 2\frac{a_z}{\omega_n^2}$ when $z_0 = 0$ and $\dot{z_0} = 0$. For a 700 km altitude Earth orbit, the maximum displacement is only 8 m with the assumption that the Earth is a perfect sphere with a radius of 6371 km. An in-plane control strategy can now be developed.

B. Attitude Dynamics

In order to explore the maneuverability of the femtosatellites for active position control, electrochromic panels are used, placed on each corner of the femtosatellites to control the solar radiation pressure by modulating the panel reflectivity. With the assumption that the center of gravity coincides with the geometric center of the femtosatellite, a differential pressure ΔF_{SRP} can generate a torque τ, shown in Figure 7, to enable attitude control. The dynamics of the femtosatellite with electrochromic panels can be investigated as a function of orientation α and from the moment of inertia I as shown in the Equation (11). Here, L is the length of femtosatellites and A_{LCD} is the total surface area of all electrochromic panels. The differential pressure is modelled at the outer edge of each panel. This will be the basis for active orbit control, so that

$$\tau = I\ddot{\alpha} \tag{11a}$$

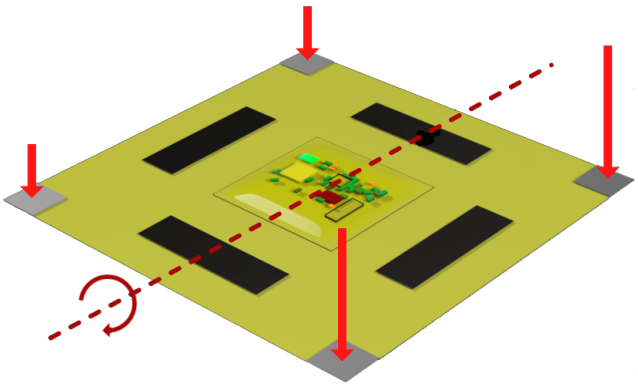

Fig. 7: Torque generated by differential SRP

and therefore

$$\Delta F_{\text{SRP}}\ \frac{1}{2}L = \frac{1}{12}mL^2\ddot{\alpha} \tag{11b}$$

and finally

$$\left(2\eta P\frac{A_{\text{LCD}}}{2}\right)\cos^2\alpha\ \frac{1}{2}L = \frac{1}{12}mL^2\ddot{\alpha} \tag{11c}$$

From Equation (11), the simplified dynamic model is shown as follows.

$$\ddot{\alpha} = \lambda\cos^2\alpha \tag{12}$$

where

$$\lambda = \frac{6\eta P A_{LCD}}{mL} \tag{13}$$

In order to represent the torque direction and magnitude that can be achieved by using electrochromic panels, a new parameter $k = [-1, 1]$ is added to Equation (12), so that

$$\ddot{\alpha} = k\lambda\cos^2\alpha \tag{14}$$

The relation between α and $\dot{\alpha}$ can be established from Equation (14) as shown in Equation (15) with details given in Appendix A-C, such that

$$\dot{\alpha}^2 = k\lambda\left[\left(\frac{\sin 2\alpha}{2} + \alpha\right) - \left(\frac{\sin 2\alpha_0}{2} + \alpha_0\right)\right] + \dot{\alpha_0}^2 \tag{15}$$

A 'bang-bang' controller for attitude angle transfer is now designed based on the attitude dynamics model. The process can be divided into two stages, when the magnitude of the $\dot{\alpha}$ is increasing and decreasing. By investigating Equation (15), the angle at the transition between these stages can be calculated; combined with Equation (14), the duration of each stage can then be estimated. In addition, the change in velocity, Δv_y, is calculated by integrating Equation (8) over the time required for each stage. A look up table (LUT) of the angle transfer and the change in velocity is then created for orbit control.

Based on the prototype femtosatellite design, the length is 0.1 m, the mass is 0.02 kg, and the total surface area of the electrochromic panels is selected as 4 cm^2. Figure 8 demonstrates the time required to change the attitude angle α between different target angles. In the extreme condition, from $-45°$ to $45°$, only 21 minutes is required to complete the manoeuvre. In addition, Figure 9 shows the influence of the total electrochromic panel surface area on the transfer time

between $0°$ and $20°$, which indicates a logarithmic relation. A balance can be found between the electrochromic panel size and the femtosatellite manoeuvrability based on the mission requirements.

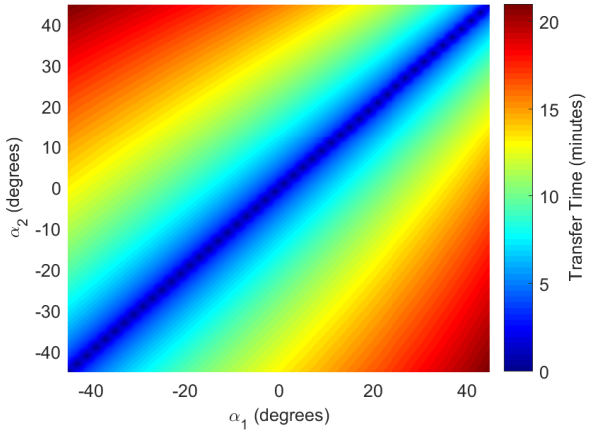

Fig. 8: Attitude angle transfer time between the α_1 and the α_2

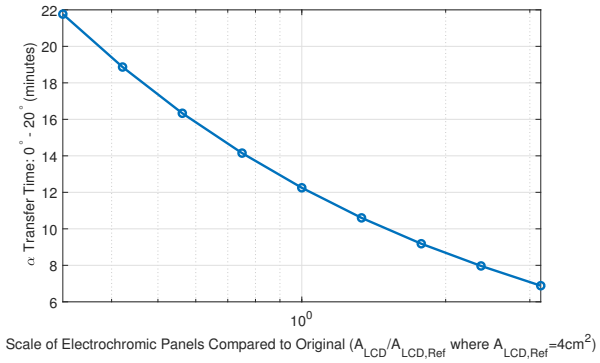

Fig. 9: Electrochromic panel scale

C. Performance Analysis

Based on the relative motion model and femtosatellite force models discussed above, an example mission scenario has been investigated for demonstration. In this mission, the maximum desired distance along the y-axis between the femtosatellites and the carrier spacecraft is set as 100 m. The femtosatellite will execute the Earth remote sensing application after release from the carrier spacecraft until reaching this distance. Once reached, the femtosatellite will apply active orbit control to maintain the desired distance, with $\dot{\bar{y}}(t)$ as described in the Equation (6), before continuing the mission. In order to better demonstrate active orbit control, only solar radiation pressure on the femtosatellite has been considered in this section. The effect of atmospheric drag on the femtosatellite and differential force between the carrier spacecraft and femtosatellite are small relative to solar radiation pressure as demonstrated in Figure 5 and 6. The normal to the femtosatellite is perpendicular to the $x-y$ plane in the relative motion coordinates during free-flying. It will rotate along the x-axis during active orbit control, therefore, an assumption of $a_x = 0$ is made as the femtosatellite is a thin panel. The dynamic model can be approximated through Equation (16), such that

$$\begin{cases} \ddot{x} - 2\omega_n \dot{y} - 3\omega_n^2 x = 0 \\ \ddot{y} + 2\omega_n \dot{x} = \dfrac{2\eta PA}{m} \cos^2\alpha \sin\alpha \\ \ddot{z} + \omega_n^2 z = \dfrac{2\eta PA}{m} \cos^3\alpha \\ \ddot{\alpha} = k\lambda \cos^2\alpha \end{cases} \tag{16}$$

The active orbit control is utilised by the 'bang-bang' controller, achieved using the parameter k in Equation (16). The femtosatellite is ejected from the carrier spacecraft with an initial speed of 1 mm/s along the y-axis in the opposite direction of the carrier spacecraft orbital motion. Figure 10 shows the simulated result in the y-axis. A detailed demonstration of the active orbit control is shown as Figure 11.

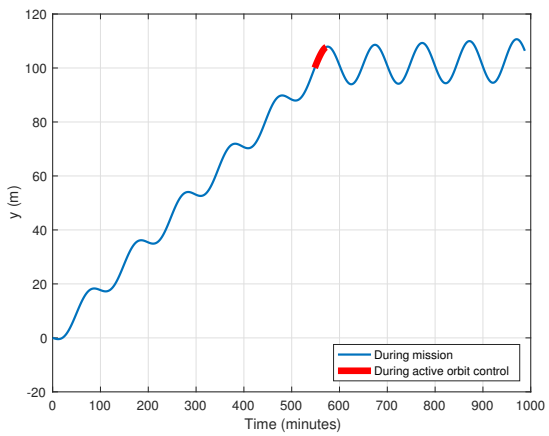

Fig. 10: Femtosatellite's distance to the carrier spacecraft along the y-axis

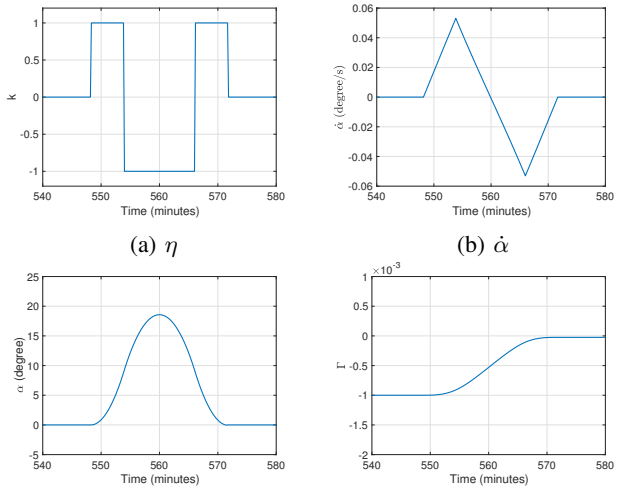

(a) η (b) $\dot{\alpha}$

(c) α (d) Γ

Fig. 11: Active orbit control (time elapsed since release from carrier spacecraft)

Figure 11a represents the direction of the differential solar radiation pressure on the electrochromic panels. Figure 11b and 11c show the femtosatellite angular velocity and attitude during active orbit control as the result of differential solar radiation pressure. These results show the acceleration and de-acceleration of the femtosatellite attitude angle α to reduce the speed in the y-axis. Γ is shown in Figure 11d, which shows the effect of the active orbit control on the femtosatellite orbit. After active orbit control, the femtosatellite enters periodic motion relative to the carrier spacecraft, as indicated by $\Gamma = 0$. For this mission, the duration of active orbit control is 23 minutes, which is equivalent to a quarter of the full orbit period. This demonstrates a smooth orbit transition from drift to periodic motion relative to the carrier spacecraft.

This example demonstrates the feasibility of using solar radiation pressure for the femtosatellite active orbit control when neglecting perturbations. By applying simple active orbit control on the femtosatellite, the swarm of femtosatellites can be manoeuvred away from the carrier spacecraft in a controlled manner to form a large sparse antenna. The operations and orbit lifetime of femtosatellite swarms are limited since ideal conditions rarely exists due to the variation of the solar cycle and atmospheric density. A mission concept is illustrated in Figure 12.

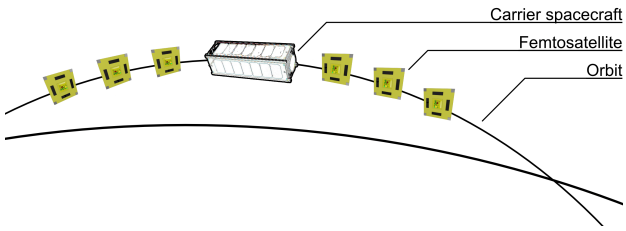

Fig. 12: Mission concept

IV. Earth Remote Sensing Application

The performance of the femtosatellites for Earth remote sensing will be characterised in this section. A swarm of those femtosatellites with active orbit control can then create an antenna array for radar applications by ensuring different distances to individual femtosatellites, as illustrated in Figure 12. A bi-static Synthetic Aperture Radar (SAR) is investigated in this paper as the Earth remote sensing application. In this application, the carrier spacecraft and femtosatellites are the transmitter and receivers respectively.

A. Signal Model

The transmitted signal s_{tx} used in the simulation is described by Equation (17) [25] such that

$$s_{tx}(t) = w_r(t) \cos\left(2\pi f_o \pm \frac{\pi B_0 t^2}{T_r}\right) \tag{17}$$

It is a function of the fast time t, which is sampled continuously. The transmit envelope is represented by w_r. The signal's carrier frequency is f_0 and bandwidth is B_0, while the range chirp pulse duration is T_r.

The demodulated received signal $s_{rx}(t, \eta)$ for a single femtosatellite in a bi-static configuration is described by Equation (18) [25] such that

$$\begin{aligned} s_{rx}(t,\eta) = \sum_{k=0}^{K-1} \Big[F_k w_a(\eta - \eta_c) w_r \left(t - \frac{R_{tx}(\eta,k) + R_{rx}(\eta,k)}{c}\right) \\ e^{-j2\pi f_o \left(\frac{R_{tx}(\eta,k)+R_{rx}(\eta,k)}{c}\right) + j\pi K_r \left(t - \frac{R_{tx}(\eta,k)+R_{rx}(\eta,k)}{c}\right)^2} \Big] \\ + n_k(t,\eta) \end{aligned} \tag{18}$$

It is a function of the fast time t and slow time η, which is sampled at the pulse repetition frequency. Moreover, η_c is the slow time stamp when the swarm is closest to the target. The scatters' identifier is k and the attenuation factor is F_k. The range from target to transmitter and receiver are represented by R_{tx} and R_{rx}. The range chirp pulse frequency is K_r. The antenna pattern is implemented by w_a and the Gaussian noise is n. White Gaussian noise is used as the noise source in this paper. Other noise distributions may occur that will affect radar performance.

B. SAR Signal Processing

Motion along the x-axis and z-axis will introduce challenges for radar signal processing due to focusing problems, requiring algorithms such as a non-linear chirp scaling method to achieve finer focusing [26]. In order to avoid the error introduced from bi-static radar algorithms and reduce the consumption time from back projection, a modified mono-static Range-Doppler algorithm (RDA) is used in this paper. This algorithm is specifically developed for this femtosatellite swarm case study. The range-Doppler algorithm is a common algorithm for SAR signal processing. It converts continuous SAR signal space to an image [25].

A block diagram of the modified RDA is shown in Figure 13. All received signals will be processed individually at the beginning via standard RDA. The first step is range compression, which converts the long transmitted pulse width to short high resolution pulse width in the range direction. Each azimuth bin is processed by a fast Fourier transform (FFT), matched filter and inverse fast Fourier transform (IFFT). Similarly, the result will be compressed in the azimuth direction. This process starts by applying azimuth FFT to each range bin to generate the range-Doppler domain. Then, the converted range-Doppler domain is processed by the range cell migration correction (RCMC) to flatten the hyperbolic range contour before matched filtering. All individually processed signals are shifted based on the relative distance in the flight direction and the radar signal round trip distance differences compared to the carrier spacecraft before being superimposed together. Finally, the azimuth IFFT is applied to generate the final image.

C. Performance Analysis

In order to evaluate the performance of the bi-static femtosatellite swarm, an example scenario has been investigated for the demonstration. The carrier spacecraft is orbiting at 700 km altitude. It is assumed that the orbit is circular with an orbital speed of 7.50 km/s. The radar pulse repetition

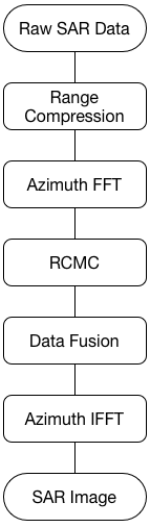

Fig. 13: Block diagram of the modified range-Doppler algorithm

frequency is 3000 Hz and lasts for a duration of 0.5 s. The swath range, which is the distance between the carrier spacecraft nadir track and the target, is 400 km. The main SAR parameters are listed in Table I. The size of the Vivaldi antenna is approximately 14.5×37 mm^2 [20].

An Airbus A380 airliner is used as the target, which is shown in Figure 14. The SAR signal space is calculated by using Equation (18) and processed by the modified range-doppler algorithm to produce the final images [25]. The position offsets between the carrier spacecraft and femtosatellites are corrected based on their position. Figure 15 is generated by using the SAR signal space without noise and positioning errors. It is used as a benchmark to compare the performance under different conditions.

TABLE I: SAR system parameters

Carrier Frequency	9.65 GHz
Bandwidth	100 MHz
Pulse Repeat Frequency	3000 Hz
Duration	0.5 s
Chirp Pulse Duration	10 μs
Orbit Altitude	700 km
Swath Range	400 km
Velocity	7.5 km/s
Approximate Range Resolution	1.5 m

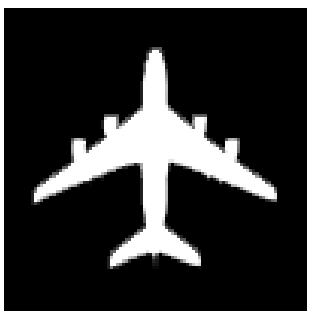

Fig. 14: Example airliner (Airbus A380)

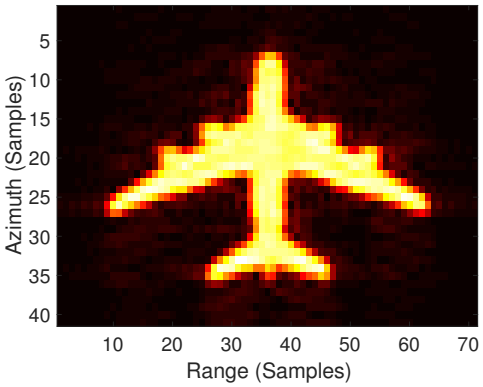

Fig. 15: SAR image benchmark

1) Test 1: Figure 16 shows images produced from different numbers of femtosatellites with -50 dB signal-to-noise ratio (SNR)[2]. With only one femtosatellite, the airliner is invisible in Figure 16a. When there are up to 20 femtosatellites, the airliner starts to appear in the images, as in Figure 16b. The more femtosatellites, the less noisy image an can be produced. The image quality is evaluated by using image peak signal-to-noise ratio. Due to the nature of the data fusion method used in the modified RDA, the image quality is proportional to the square root of the number of femtosatellites, as shown in Figure 17. However, in the worst-case scenario when the airliner is completely invisible. The image SNR will reach noise saturation as the low raw signal SNR results in loss of sensitivity. This test uses Gaussian white noise as an example for demonstration under optimistic conditions. In reality, the sources of noise are more complicated and requires further research to be fully investigated.

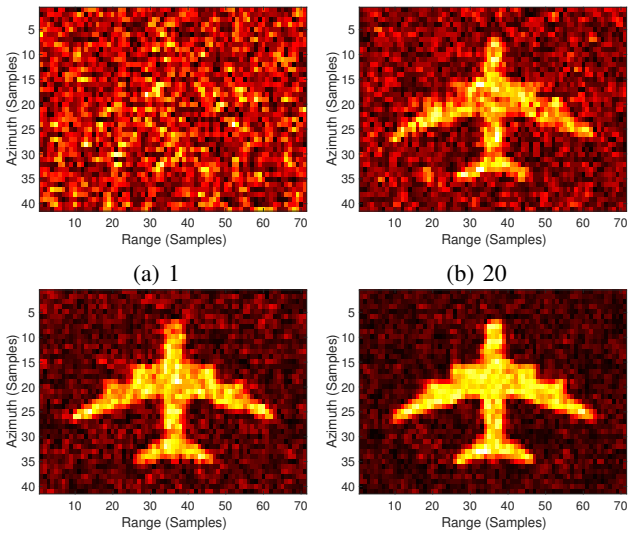

(a) 1 (b) 20

(c) 50 (d) 100

Fig. 16: Radar image produced with different number of femtosatellites

[2]SNR is the ratio between the power of the raw SAR signal and the power of the added Gaussian noise.

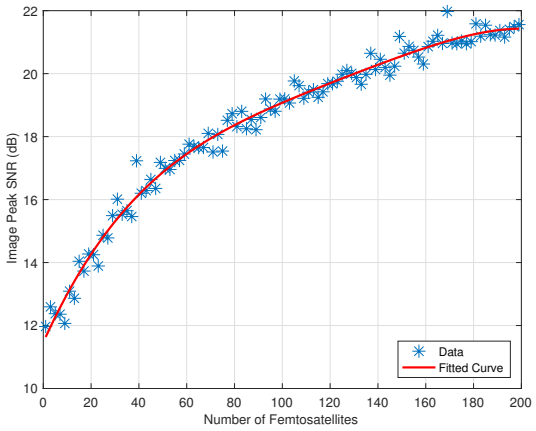

Fig. 17: Image peak SNR against number of femtosatellites

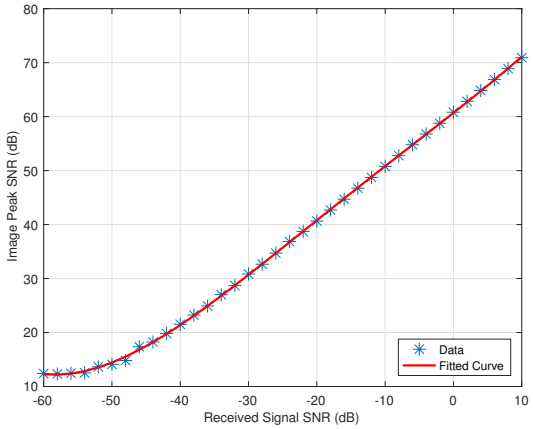

Fig. 19: Image peak SNR against received signal SNR

2) Test 2: Figure 18 shows the processed images with different signal-to-noise ratios. All images are processed based on the signal space from 20 femtosatellites. Figure 18a presents a similar result with -30 dB SNR as the benchmark in Figure 15. As the SNR reduces, the airliner becomes less visible and hard to identify. The target is undetectable when SNR reaches -60 dB. The image quality will be saturated at low SNR, as shown in Figure 19.

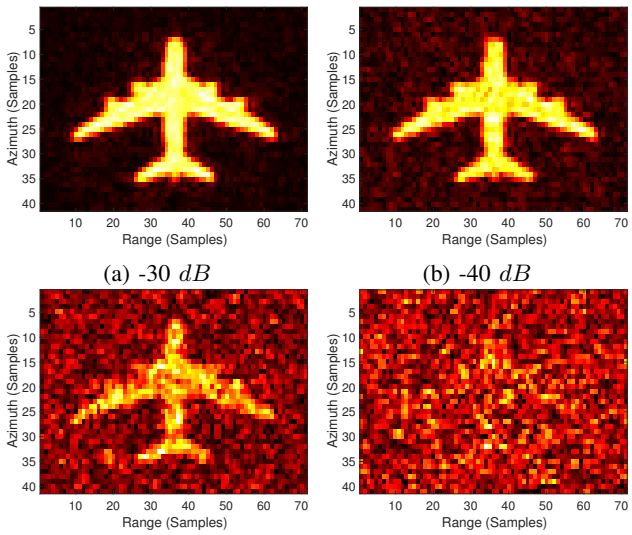

(a) -30 dB (b) -40 dB

(c) -50 dB (d) -60 dB

Fig. 18: Radar image produced with different received signal SNR

3) Test 3: In real-world scenarios, position errors will be present which will degrade the performance of the system. This will lead to an offset of the target in the final radar image. Figure 20 shows the effect of this error on processed radar images. All images are processed based on the signal space from 20 femtosatellites with -30 dB SNR. The processed radar image indicates an acceptable result with 2 m error, as shown in Figure 20b. The image is clearly blurred when the positioning error is 5 m. The image SNR flattens as positioning error increases and the boundary is proportional to the size of the target and the resolution of the radar. In Figure 20d, the target will be extremely hard to identify. While orbit determination is beyond the scope of the paper it is clear that accurate position determination is key, which may require on-board processing on the carrier spacecraft.

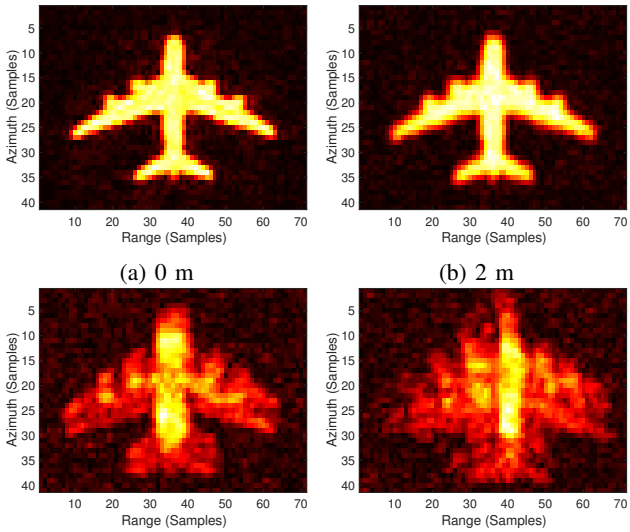

(a) 0 m (b) 2 m

(c) 5 m (d) 10 m

Fig. 20: Radar image produced with different positioning errors

The effect of positioning error and SNR are shown in Figure 21. The image SNR has a steady drop as the positioning error increases unless it reaches a noise saturation at 12 dB where the target is completely invisible. With higher SNR, the target remains detectable but no longer identifiable when the positioning error increases. This plot can be used to estimate the expected radar image quality from the bi-static femtosatellite swarm with a given system specification.

V. Conclusion

In this paper, a novel concept for Earth remote sensing using solar radiation pressure enabled femtosatellites has been

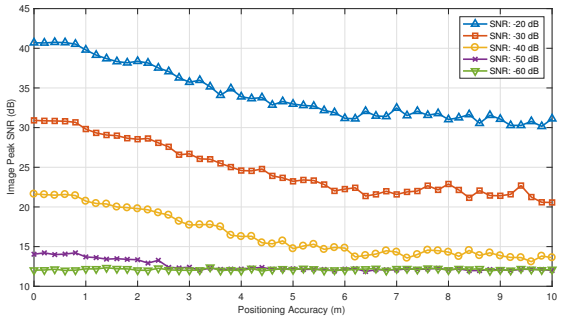

Fig. 21: Image peak SNR

proposed to explore the mission capability of a femtosatellite swarm. The prototype design features a low-cost, high area-to-mass ratio concept. The mission is based on a Sun-synchronous orbit to maximise solar power generation and take advantage of solar radiation pressure for orbit control. A relative motion model and force model have been introduced to estimate the motion of the femtosatellites. An example scenario of using active orbit control to position the femtosatellites has been presented. The potential of using femtosatellites as receivers is shown via an Earth remote sensing application which is simulated by using a SAR model. This provides a method to estimate the swarm performance under given conditions. In addition to Earth remote sensing, a bi-static femtosatellite swarm could be used for target detection, such as ships with AIS turned off or airliners with their beacon turned off. With femtosatellite swarms, bi-static SAR performance could be improved by lowering noise. This could also reduce the radar system mass and cost. The femtosatellite concept in this paper could be improved by optimizing the femtosatellite design, the swarm distribution pattern, and using a dynamic model with other perturbations and noise sources. Bi-static SAR performance could be further improved by applying advanced signal processing algorithms which will be investigated in future work.

ACKNOWLEDGEMENT

This work was supported by the Engineering and Physical Sciences Research Council (EPSRC) Grant number EP/K014307/1; and the MOD University Defence Research Collaboration (UDRC) in Signal Process.

APPENDIX A
FORCE MODEL

A. Solar Radiation Pressure

The effect of solar radiation pressure on each femtosatellite can be illustrated as shown in Figure 22. The projected area, A_{proj}, of a femtosatellite is given by

$$A\cos\alpha \tag{19}$$

Therefore, the SRP acceleration applied on the femtosatellite surface normal direction becomes

$$\frac{2\eta PA}{m}\cos^2\alpha \tag{20}$$

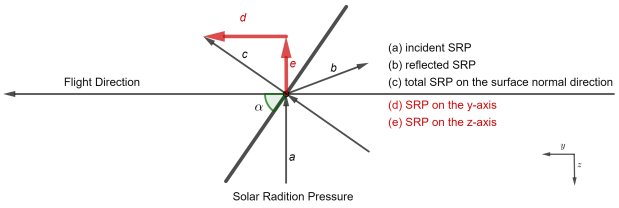

Fig. 22: Force model - solar radiation pressure

When split into the y-axis and the z-axis, this becomes

$$\frac{2\eta PA}{m}\cos^2\alpha\sin\alpha \tag{21}$$

and

$$\frac{2\eta PA}{m}\cos^3\alpha \tag{22}$$

B. Atmospheric Drag

The projected area, A', of a femtosatellite is given by

$$A' = A|\sin\alpha| \tag{23}$$

The drag and lift forces on the femtosatellite [23], [24] are:

$$\begin{cases} F_{\text{Drag}} = -\dfrac{1}{2}c_D A'\rho v_{\text{rel}}^2 \\ F_{\text{Lift}} = -\dfrac{1}{2}c_L A'\rho v_{\text{rel}}^2 \end{cases} \tag{24}$$

where, assuming a Newtonian approximation with free molecular flow and specular reflection of molecules [23], the drag and lift coefficients, c_D and c_L respectively, are:

$$\begin{cases} c_D = c_{D,normal}\sin^2\alpha \\ c_L = c_{D,normal}\sin\alpha\cos\alpha \end{cases} \tag{25}$$

With $c_{D,normal} = 2$, so that, the drag in the y-axis and lift in the z-axis become

$$\begin{cases} a_{y,\text{AD}} = -\dfrac{A}{m}\rho v_{\text{rel}}^2|\sin\alpha|\sin^2\alpha \\ a_{z,\text{AD}} = -\dfrac{A}{m}\rho v_{\text{rel}}^2|\sin\alpha|\sin\alpha\ \cos\alpha \end{cases} \tag{26}$$

C. Derivation of Equation 15

From Equation 14 it can be seen that

$$\frac{d\dot{\alpha}}{dt} = k\lambda\cos^2\alpha \tag{27}$$

so that

$$\frac{d\alpha}{dt}\frac{d\dot{\alpha}}{d\alpha} = k\lambda\cos^2\alpha \tag{28}$$

and therefore

$$\dot{\alpha}\frac{d\dot{\alpha}}{d\alpha} = k\lambda\cos^2\alpha \tag{29}$$

Equation 29 can then be written as

$$\dot{\alpha}d\dot{\alpha} = k\lambda\cos^2\alpha d\alpha \tag{30}$$

and integrating on both sides

$$\int_{\dot{\alpha}_0}^{\dot{\alpha}}\dot{\alpha}d\dot{\alpha} = \int_{\alpha_0}^{\alpha}k\lambda\cos^2\alpha d\alpha \tag{31}$$

$$\frac{1}{2}\dot{\alpha}^2\Big|_{\dot{\alpha_0}}^{\dot{\alpha}} = \frac{1}{2}k\lambda(\frac{\sin 2\alpha}{2}+\alpha)\Big|_{\alpha_0}^{\alpha} + C \tag{32}$$

$$\dot{\alpha}^2 - \dot{\alpha_0}^2 = k\lambda(\frac{\sin 2\alpha}{2}+\alpha-\frac{\sin 2\alpha_0}{2}-\alpha_0) + C \tag{33}$$

Finally, when $\dot{\alpha} = \dot{\alpha_0}$ and $\alpha = \alpha_0$, $C = 0$ so that,

$$\dot{\alpha}^2 = k\lambda(\frac{\sin 2\alpha}{2}+\alpha-\frac{\sin 2\alpha_0}{2}-\alpha_0) + \dot{\alpha_0}^2 \tag{34}$$

REFERENCES

[1] Morrow, W. E. and Rogers, T. F., "The West Ford Experiment," Proceedings of the IEEE, vol.52, no.5, 1964, pp.461-468.

[2] Keller, J. interview of Joshi, A., "Startup to Develop Satellite-On-A-Chip," Military & Aerospace Electronics, February 1994.

[3] Huang, A., Hansen, W. W., Janson, S. W. and Helvajian H., "Development of a 100gm Class Inspector Satellite Using Photostructurable Glass/Ceramic Materials," Proc. of SPIE, vol. 4637, 2002, pp. 297-304.

[4] Barnhart, D. J., Vladimirova, T. and Sweeting, M. N., "Very Small Satellite Design for Space Sensor Networks," AIAA Journal of Spacecraft and Rockets, vol. 46, no. 2, Mar.-Apr. 2009, pp. 469-472.

[5] Johnson, M., Manchester, Z., Peck, M.,"KickSat, an Open Source ChipSat Dispenser and Citizen Space Exploration Proof of Concept Mission," 4th European CubeSat Symposium, Brussels, Belgium, 2012.

[6] Tristancho, J. and Gutierrez-Cabello, J., "A probe of concept for femto-satellites based on commercial-of-the-shelf," IEEE/AIAA 30th Digital Avionics Systems Conference, Seattle, US, 2011.

[7] McInnes, C. R.,"Solar sailing: technology, dynamics and mission applications," Springer Praxis, London, 1999, Chapter 2.

[8] Mingotti, G., McInnes, C. R.,"High Area-to-Mass Ratio and Small Length-Scale Spacecraft Formation Flying Applications" 24th AAS/AIAA Space Flight Mechanics Meeting, 2014, AAS-14-215.

[9] Lücking, C., Colombo, C., McInnes, C. R., "Orbit Control of High Area-to-mass Ratio Spacecraft Using Electrochromic Coating," 61st International Astronautical Congress, Prague, Czech Republic, Oct 2010.

[10] Colombo, C., Lücking, C., McInnes, C. R., "Orbit Evaluation, Maintenance and Disposal of SpaceChip Swarms Through Electro-chromic Control," Acta Astronautica 82.1, 2013, pp.25-37.

[11] Cao,J. , Clemente, C., McInnes, C. R., Soraghan, J. J., Uttamchandani, D., "A Novel Concept for Earth Remote Sensing Using a Bistatic Femto-Satellite Swarm in Sun Synchronous Orbit," 66th International Astronautical Congress, Jerusalem, Israel, Oct 2015, IAC-15,B4,6B,4,x28594.

[12] Wiley, C. A., "Synthetic Aperture Radars: A paradigm for Technology Evolution," IEEE Transactions on Aerospace and Electronic Systems, vol.AES-21, no.3, 1985, pp.440-443.

[13] D'Errico, M., Grassi, M., Vetrella, S., "A bistatic SAR mission for earth observation based on a small satellite," Acta Astronautica, vol.39, no.9, 1996, pp.837-846.

[14] Iervolino, P., Guida, R., Whittaker, P., "Novasar-S and maritime surveillance," IEEE International Geoscience and Remote Sensing Symposium, Melbourne, VIC, 2013.

[15] Krieger, G. et al., "TanDEM-X: A Satellite Formation for High-Resolution SAR Interferometry," IEEE Transactions on Geoscience and Remote Sensing, vol.45, no.11, pp.3317-3341, 2007.

[16] Sugimoto, Y., Ozawa, S., Inaba, N., "Spaceborne Synthetic Aperture Radar Signal Processing Using Field-Programmable Gate Arrays," Journal of Applied Remote Sensing, 12(3), 035007, 2018.

[17] Walterscheid, I., Ender, J. H. G., Brenner, A. R. and Loffeld, O., "Bistatic SAR Processing and Experiments," IEEE Transactions on Geoscience and Remote Sensing, vol.44, no.10, 2006, pp.2710-2717.

[18] Schwegmann, C. P., Kleynhans, W., Salmon, B. P., "Synthetic Aperture Radar Ship Detection Using Haar-Like Features," IEEE Geoscience and Remote Sensing Letters, vol.14, no.2, 2017, pp.154-158.

[19] Tristancho, J., "Simplified Femto-satellite Operations for Disaster Management Missions," 63rd International Astronautical Congress, Naples, Italy, 2012, IAC-12,B4,3,12,x15631.

[20] Mandeville, A. and Jackson, R. W., "Surface Mount End-Fire Antenna Package," Electronics Letters, vol.45, no.7, 2009, pp.340-342.

[21] Vallado, D., "Fundamentals of Astrodynamics and Application," Second Edition, Kluwer Academic Publishers, 2001.

[22] Weis, L. and Peck, M., "Active Solar Sail Designs for Chip-scale Spacecraft," 28th Annual AIAA/USU Conference on Small Satellites, 2014.

[23] Sowter, A., "Drag coefficients with applications to satellite orbits," Ph.D. dissertation, Aston University, UK, 1989.

[24] Horsley, M., Nikolaev, S., Pertica, A., "Rendezvous Maneuvers of Small Spacecraft Using Differential Lift and Drag," Journal of Guidance, Control, and Dynamics, 2011.

[25] Cumming, I. G. and Wong, F. H., "Digital Processing of Synthetic Aperture Radar Data, Algorithms and Implementation," Artech House, Boston, 2005.

[26] Wong, F. H., Cumming, I. G., Neo, Y. L., "Focusing Bistatic SAR Data Using the Nonlinear Chirp Scaling Algorithm," IEEE Transactions on Geoscience and Remote Sensing, vol.46, no.9, 2008, pp.2493-2505.

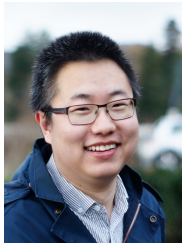

Jianlin Cao was born in Tianjin, China. He received BEng (Hons.) in the Electronics and Electrical Engineering from University of Strathclyde, Glasgow, UK, in 2013. He is currently pursuing the PhD degree in Mechanical and Aerospace Engineering and working as Electro-Mechanical Engineering in University of Strathclyde. His research interests include small satellites, unmanned aerial vehicle monitoring, synthetic aperture radar system, non-destructive evaluation, and robot systems.

Carmine Clemente (S09-M13-SM18) received the Laurea cum laude (BSc) and Laurea Specialistica cum laude (MSc) degrees in telecommunications engineering from Universita degli Studi del Sannio, Benevento, Italy, in 2006 and 2009, respectively. In 2012, he received the Ph.D. degree in the Department of Electronic and Electrical Engineering, University of Strathclyde, Glasgow, UK. Currently he is a Senior Lecturer in the Department of Electronic and Electrical Engineering, University of Strathclyde, Glasgow, U.K working on advanced Radar signal processing algorithm, MIMO radar systems and micro-Doppler analysis. His research interests include synthetic aperture radar (SAR) focusing and bistatic SAR focusing algorithms development, micro-Doppler signature analysis and extraction from multistatic radar platforms, micro-Doppler classification and statistical signal processing.

Colin R. McInnes is James Watt Chair, Professor of Engineering Science at the University of Glasgow. His research interests include spacecraft orbital dynamics, solar sailing, space resources and other advanced space concepts. His work is currently supported by a Royal Academy of Engineering Chair in Emerging Technologies and a Royal Society Wolfson Research Merit Award.

John J. Soraghan (S83-M84-SM96) received the B.Eng. (Hons.) and M.Eng.Sc. degrees in electronic engineering from University College Dublin, Dublin, Ireland, in 1978 and 1983, respectively, and the Ph.D. degree in electronic engineering from the University of Southampton, Southampton, U.K., in 1989. His doctoral research focused on synthetic aperture radar processing on the distributed array processor. After graduating, he worked with the Electricity Supply Board in Ireland and with Westinghouse Electric Corporation in the U.S. In 1986, he joined the Department of Electronic and Electrical Engineering, University of Strathclyde, Glasgow, U.K as a lecturer. He was a Manager of the Scottish Transputer Centre from 1988 to 1991, Manager with the DTI Parallel Signal Processing Centre from 1991 to 1995 and Head of the ICSP from 2005-2007. He became a Professor in Signal Processing in 2003 and held the Texas Instruments Chair in Signal Processing from 2004-2016.

He is currently the Director of the Sensor Signal Processing Research Groups within the Centre for Signal and Image Processing (CeSIP) at Strathclyde.